Supporting information: Cross-examining polyurethane nanodomain formation and internal structure

Maxwell W. Terban,[*,†] Karsten Seidel,[‡] Elmar Pöselt,[¶] Marc Malfois,[§] Roelf-Peter Baumann,[‡] Ralf Sander,[‡] Dirk Paulus,[‡] Bernd Hinrichsen,[‡] and Robert E. Dinnebier[†]

†*Max Planck Institute for Solid State Research, Heisenbergstr. 1, 70569 Stuttgart, Germany*

‡*BASF SE, Carl-Bosch-Str. 38, 67056 Ludwigshafen, Germany*

¶*BASF Polyurethanes GmbH, Elastogranstr. 60, 49448 Lemförde, Germany*

§*ALBA Synchrotron, Carrer de la Llum 2-26, 08290 Cerdanyola del Vallès, Barcelona, Spain*

E-mail: M.Terban@fkf.mpg.de

Contents

1 Atomic force microscopy (AFM) 2

1.1 Semi-quantitative analysis of AFM images 2

2 Transmission electron microscopy (TEM) 7

3 Small-angle x-ray scattering (SAXS) 8

3.1 Analysis of SAXS curves 8

4 Wide-angle x-ray scattering (WAXS) and total scattering measurements 11

4.1 Laboratory 11

4.2 ALBA synchrotron 11

4.3 Advanced photon source (APS) 11

4.4 European synchrotron radiation facility (ESRF) 12

4.5 Data processing 12

4.6 X-ray data comparison 14

4.7 Assessment of local structure in the PDFs 16

4.8 Experimental resolution effects 21

4.9 Estimation of PDF attenuation profiles from AFM 24

5 Solid-state nuclear magnetic resonance (SSNMR) 25

References 27

1 Atomic force microscopy (AFM)

For characterizing the morphology of sample cross-sections, the AFM Dimension ICON (Bruker) was used. The cross-sections were prepared by cryo-microtome at -80 °C. AFM measurements were performed in Tapping Mode, collecting the topographical Height Image and corresponding Phase Image (material contrast) of 1×1 µm^2 areas.

1.1 Semi-quantitative analysis of AFM images

To compare the AFM phase contrast images on a semi-quantitative basis, the software ImageJ was used with the NanoDefine plugin, Particle Sizer.[1,2] A bandpass filter was used to smooth the image, then a brightness threshold was used to highlight areas approximately representative of the hard domains. All surrounding areas were then masked for maximal contrast. The Particle Sizer plugin was run on the masked images. Since the domains are

highly anisotropic, they were assessed by the distribution of maximum and minimum Feret diameters obtained from the fitted domains in each TPU sample image. As the borders of the domains are not well defined, and the Feret diameters do not necessarily account for the full complexity of the domain shapes, values obtained from this analysis should only be taken as relative for comparison between samples. Furthermore, AFM images are a 2D representation of the TPU 3D (hierarchy of) structure(s), resulting from the random cut via cryo-microtomy (should be normally distributed). It is more difficult to account for process related anisotropies (not normal). The steps in image processing and resulting size distributions are shown in Figures S1, S2, and S3. A log-normal distribution was fit to the aggregate distributions, and the refined parameters are shown in Table S1.

Table S1: Refined parameters for log-normal distributions.

Sample	HS	SS	Mean	Variance	Skew	Kurtosis	Standard Dev.
TPU-06	HDI	ether	24.2	432.4	3.7	31.5	20.8
TPU-15	MDI	ether	16.5	119.9	2.6	13.6	11.0
TPU-30	MDI	ester	29.4	1674.0	8.8	273.0	40.9

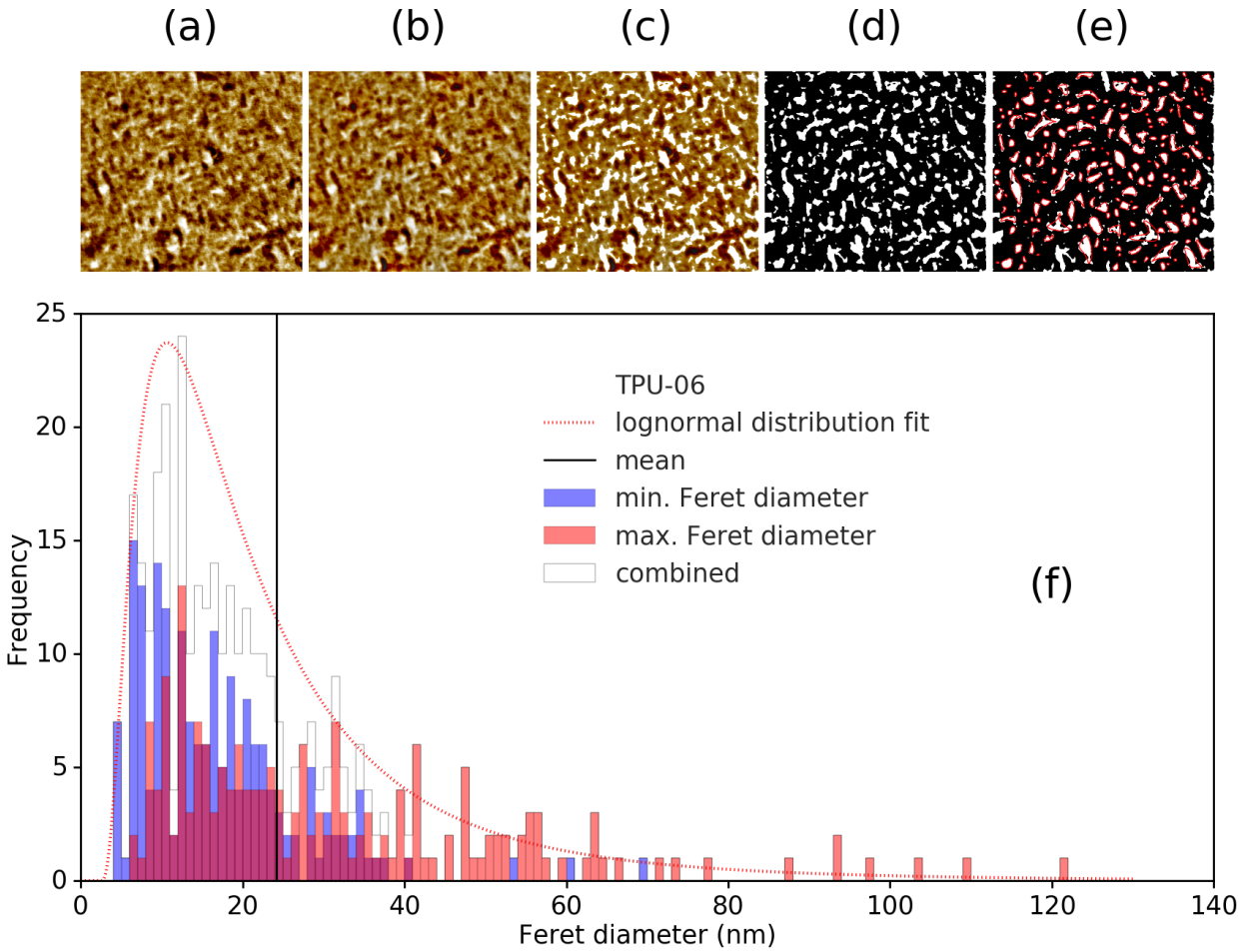

Figure S1: (a-e) AFM image processing steps for TPU-06. (f) distribution of minimum and maximum Feret diameters.

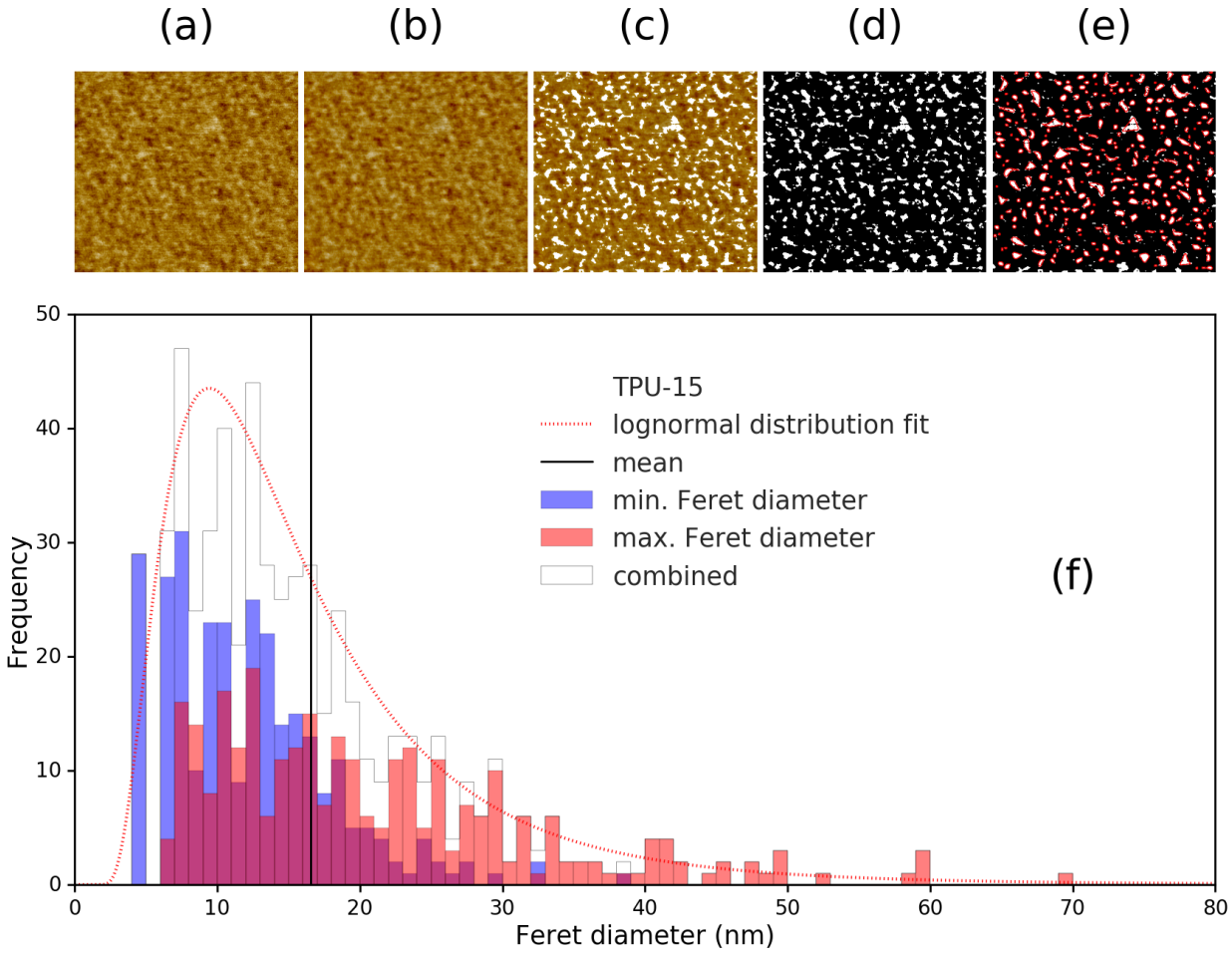

Figure S2: (a-e) AFM image processing steps for TPU-15. (f) distribution of minimum and maximum Feret diameters.

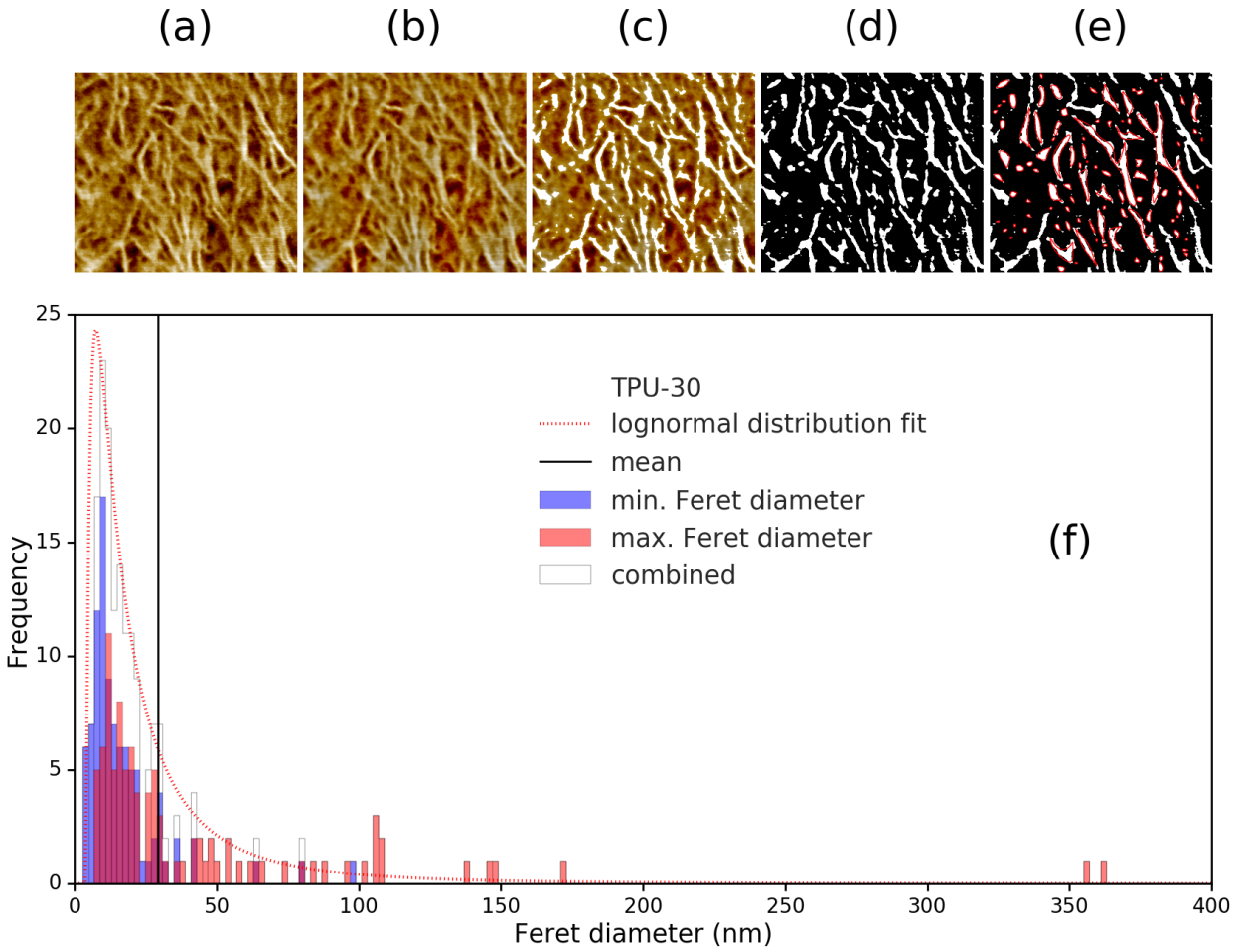

Figure S3: (a-e) AFM image processing steps for TPU-30. (f) distribution of minimum and maximum Feret diameters.

2 Transmission electron microscopy (TEM)

Morphology was investigated with transmission electron microscopy. Ultrathin cross-sections were prepared via cryo-ultramicrotomy (Leica UC 7), which were stained with RuO_4 from the vapor phase. The samples were examined using a Zeiss Libra 120 microscope equipped with an omega filter operating at an accelerating voltage of 120 kV in elastic mode. RuO_4 lends contrast between amorphous and crystalline regions of semicrystalline polymers, leading to a bright appearance of crystalline lamellae in TEM images.

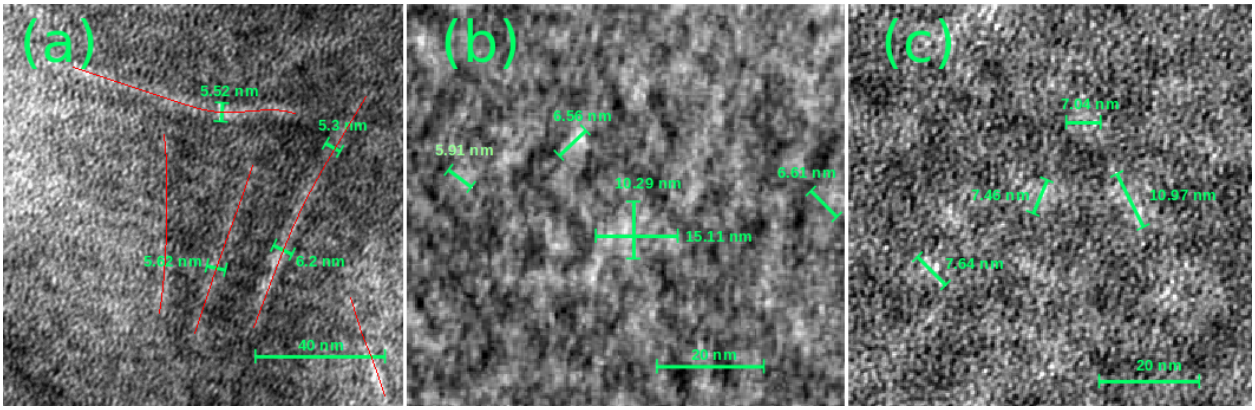

Figure S4: Zoomed-in view of the domain structures observed by TEM in (a) TPU-30, (b) TPU-06, and (C) TPU-15, stained with RuO_4 respectively. Representative features and dimensions are marked in red or green.

3 Small-angle x-ray scattering (SAXS)

SAXS experiments were conducted at the NCD-SWEET beamline (BL11) at ALBA Synchrotron in Barcelona, Spain. Data were collected using an x-ray energy of 12.40 keV (λ = 0.9999 Å) and a Pilatus 1M detector from Dectris (981 × 1043 pixels, 172 × 172 μm^2 each) mounted orthogonal to the beam path at a distance of 7.6498 m from the sample. Silver behenate (AgBH) was used as a calibration standard.

3.1 Analysis of SAXS curves

Diffraction in SAXS can be attributed to constructive interference between x-rays scattered from segregated regions of like density. Single peaks observed in paracrystalline and semicrystalline polymers (including thermoplastic polyurethanes), are often attributed to microphase segregated crystalline and amorphous (or hard and soft) regions, often in the form of lamellar stacks[3–6] or a random close-packed or liquid-like distribution of segregated domains.[7] For a 3D isotropic material (e.g., random close-packed or liquid-like), the position of the peak in the observed SAXS intensities, $I(Q)$, can be related to the interdomain spacing d by the the Bragg relationship, i.e., $d = 2\pi/Q$.[8,9] If isotropic SAXS intensities are instead assumed to arise from an orientationally averaged distribution of microdomains consisting of 1D lamellar stacks, then the so-called Lorentz correction is recommended where the intensity from the 1D stacks, I_{1D}, is related to the observed isotropic intensities by $I_{\mathsf{1D}} \propto Q^2 I(Q)$, and then d should be assessed from the maximum in $Q^2 I(Q)$.[8,10]

SAXS data are commonly assessed by various forms of real-space distribution functions, which come with different requirements for the validity of their use and varying benefits for assessing different physical properties of structural heterogeneities[4,11–14] The most common forms are the 3D and 1D correlation functions. These functions represent the local fluctuation in the phase density with respect to the average and are related to the probability that a rod of length r will have both ends in the same phase. The 3D correlation function corresponds

to the case of isotropic materials, and can be calculated by

$$\Gamma_3(r) = \frac{1}{Q^*}\int_0^\infty Q^2 I(Q)\frac{\sin(Qr)}{Qr}dQ \tag{1}$$

where Q^* is the SAXS invariant, defined by $Q^* = \int_0^\infty Q^2 I(Q)dq$. The 1D correlation function corresponds to the case of scattering from orientationally averaged 1D stacks and can likewise be calculated from

$$\Gamma_1(r) = \frac{1}{Q^*}\int_0^\infty Q^2 I(Q)\cos(Qr)dQ. \tag{2}$$

Other common real-space functions used to assess SAXS data are the chord distribution function, $g(r)$ (3D isotropic case),[11] and the interface distribution function, $g_1(r)$ (1D stacks),[4,5] which are respectively related to the second derivatives of the 3D and 1D correlation functions.

We used the software SasView (http://www.sasview.org/) to calculate $\Gamma_3(r)$, $\Gamma_1(r)$, and $g_1(r)$ from the SAXS for the three samples. To reduce termination effects, the program extrapolates the data to $Q = 0$ using the Guinier relationship, and to $Q = \infty$ using Porod's law, with corrections for positive deviations caused by thermal density fluctuations and negative deviations caused by diffuse phase boundaries.[8] A real-space PDF, $G(r)$ was also extracted from the SAXS data by processing the data using the formalism for total scattering data using the program xPDFsuite[15] (see PDF section below, use of this program on SAXS shares similarities to the automated reduction methods described by A. Stribeck[10]). The different real-space functions obtained from the SAXS data are compared in Fig. S5. The SAXS data were also assessed in reciprocal space by fitting a pseudo-Voigt function to both as-measured ($I(Q)$) and Lorentz-corrected ($Q^2I(Q)$) datasets. Interdomain spacings were estimated from the peak positions in the reciprocal- and real-space functions, Table S2. The average domain size was further estimated from extension of the linear decreasing portion of Γ_3 to the minimum (TPU-06: 4.4 nm, TPU-15: 3.5 nm, TPU-30: 4.3 nm).

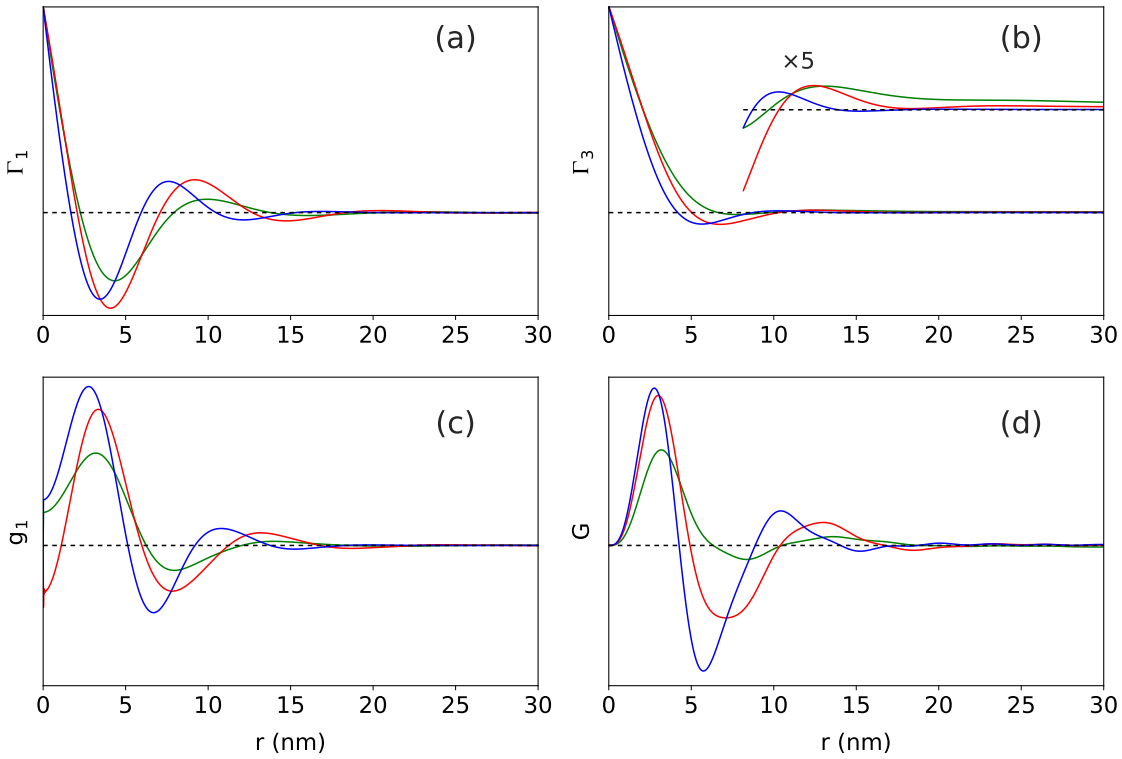

Figure S5: Comparison of different real-space functions obtained from SAXS measured from TPU-30, TPU-06, and TPU-15: (a) 1D correlation function Γ_1, (b) 3D correlation function Γ_3, 1D interface distribution function g_1, and the pair distribution function obtained from xPDFsuite.

Table S2: Comparison of structural parameters estimated from SAXS data.

Sample	Parameter	3D		1D	
		$I(Q)$	Γ_3	$Q^2I(Q)$	Γ_1
TPU-06	d_{lp} (nm)	11.2	12.7	9.9	9.3
TPU-15	d_{lp} (nm)	9.3	10.5	8.2	7.8
TPU-30	d_{lp} (nm)	14.0	13.3	10.8	10.1

4 Wide-angle x-ray scattering (WAXS) and total scattering measurements

4.1 Laboratory

Laboratory XRPD patterns were collected at room temperature on a STOE Stadi P diffractometer with CuKα_1 radiation (λ = 1.540596 Å), using a Ge(111) Johann monochromator and a Mythen 1K detector in transmission geometry. For laboratory measurements, a standard was prepared in the same geometry as the TPU pellets. A powdered mixture of 10 wt% Si and 90 wt% polyamide 6 (PA6) as filler (to avoid significant absorption effects) was prepared and then compacted using a pellet press into a disc of 2 mm height and 6 mm diameter.

4.2 ALBA synchrotron

WAXS were conducted at the NCD-SWEET beamline (BL11) at ALBA synchrotron in Barcelona, Spain. Data were collected using an x-ray energy of 12.40 keV (λ = 0.9999 Å) and a LX255-HS detector from Rayonix (960 × 2880 pixels, 88 × 88 μm^2 each) mounted orthogonal to the beam path at a distance of 122.98 mm from the sample. Cr_2O_3 was used as a calibration standard.

4.3 Advanced photon source (APS)

X-ray total scattering measurements were conducted using beamline 11-ID-B of APS at Argonne National Laboratory (ANL), in Chicago, USA. Data were collected in rapid acquisition mode[16] using an x-ray energy of 58.68 keV (λ = 0.2113 Å) and a 2D PerkinElmer detector (2048 × 2048 pixels, 200 × 200 μm^2 each) mounted orthogonal to the beam path at a distance of 166.31 mm from the sample. Pellet samples were measured at room temperature in transmission geometry. Scattering contributions from air and the sample holder were measured and subtracted. CeO_2 NIST 674b was used as a calibration standard.

4.4 European synchrotron radiation facility (ESRF)

Additional total scattering experiments were conducted using beamline ID31 at the ESRF in Grenoble, France. Data were collected in rapid acquisition mode using an x-ray energy of 68.54 keV ($\lambda = 0.1809$ Å) and a Pilatus3 X CdTe 2M from Dectris (1475 × 1679 pixels, 172 × 172 μm^2 each) mounted orthogonal to the beam path at a distance of 273.38 mm from the sample. Pellet samples were measured at room temperature in transmission geometry. Scattering contributions from air and the sample holder were measured and subtracted. CeO_2 NIST 674b was used as a calibration standard.

4.5 Data processing

Calibration of the detector geometry and image integration were performed using the azimuthal integration software pyFAI.[17] The raw data images were summed and corrected for polarization effects, then masked and azimuthally integrated to produce 1D powder diffraction patterns. Further normalization and transformation to the real space PDF was performed using PDFgetX3,[18] within xPDFsuite.[15] The total scattering structure function S(Q) is obtained from the coherent scattering intensities $I_c(Q)$, after removal of the self-scattering by,

$$S(Q) = \frac{I_c(Q) - N\langle f(Q)^2\rangle + N\langle f(Q)\rangle^2}{N\langle f(Q)\rangle^2}. \tag{3}$$

Q is the magnitude of the scattering momentum transfer ($Q = 4\pi \sin(\theta)/\lambda$ for elastic scattering, where λ is the wavelength, and 2θ is the scattering angle). $f_i(Q)$ is the atomic form factor for atom i, and averaging denoted by $\langle . \rangle$ is performed stoichiometrically over all atoms (N) in the sample. The experimental PDF, $G(r)$, is obtained via truncated Fourier transformation of the reduced total structure function $F(Q) = Q\,(S(Q) - 1)$, by

$$G(r) = \frac{2}{\pi} \int_{Q_{\min}}^{Q_{\max}} F(Q) \sin(Qr)\, \mathrm{d}Q, \tag{4}$$

which corresponds to the real space density distribution by

$$G(r) = 4\pi r \left[\rho(r) - \rho_0 \gamma_0\right], \tag{5}$$

where ρ_0 is the average atomic number density and $\rho(r)$ is the local atomic pair density, which is the average density of neighboring atoms at a distance r from an atom at the origin. γ_0 is the characteristic function of the diffracting domains which equals 1 for bulk crystals, but has an r-dependence for nano-sized domains.[19] The range of diffraction data used in the Fourier transform depended on the measurable range of the instrument (radiation source/detector), and the data quality. $F(Q)$ is typically truncated below the instrumental in order to reduce the effects of noise at high-Q on the resulting PDFs. In certain cases, it may be beneficial to apply modification functions to the Fourier kernel, $F(Q)$ prior to transformation, which can help to reduce the effects of noise and finite termination. The function can be applied as $F'(Q) = M(Q)F(Q)$, where $F'(Q)$ replaces $F(Q)$ in equation 2. $M(Q)$ is then defined by a smoothly varying function, commonly using a Lorch function, given by,

$$M(Q) = \frac{\sin(Q\Delta)}{Q\Delta} \tag{6}$$

where $\Delta = \pi/Q_{max}$.[20] In the analysis herein, Lorch-type modifications were used when explicitly noted (e.g. for removing nonstructural, low-amplitude/high-frequency contributions from synchrotron data to help validate the use of CuKα_1 source radiation for measuring density distributions within the domain). Structure refinement to the PDFs can be performed for example in either PDFgui[21] or TOPAS v6.[22] Here, peak fitting analysis was carried out using home written code in Python.

4.6 X-ray data comparison

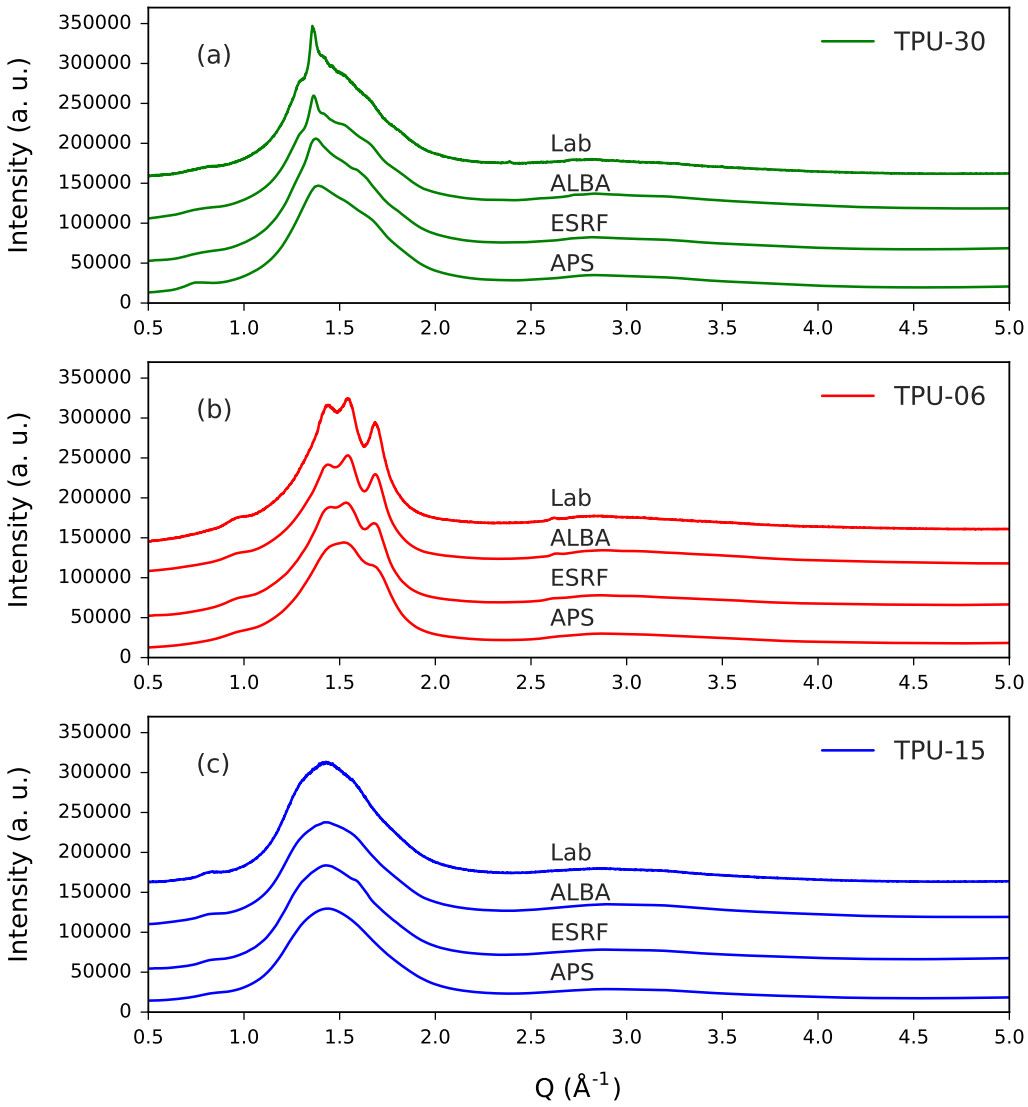

Figure S6: Comparison of WAXS diffraction patterns obtained from different measurements. Differences in Q-resolution, due to different experimental setups, detectors, and x-ray energies, are apparent by the relative sharpness of the diffraction features. The best resolution of features for these samples was achieved with the laboratory data using the Mythen 1K detector and CuKα_1 radiation.

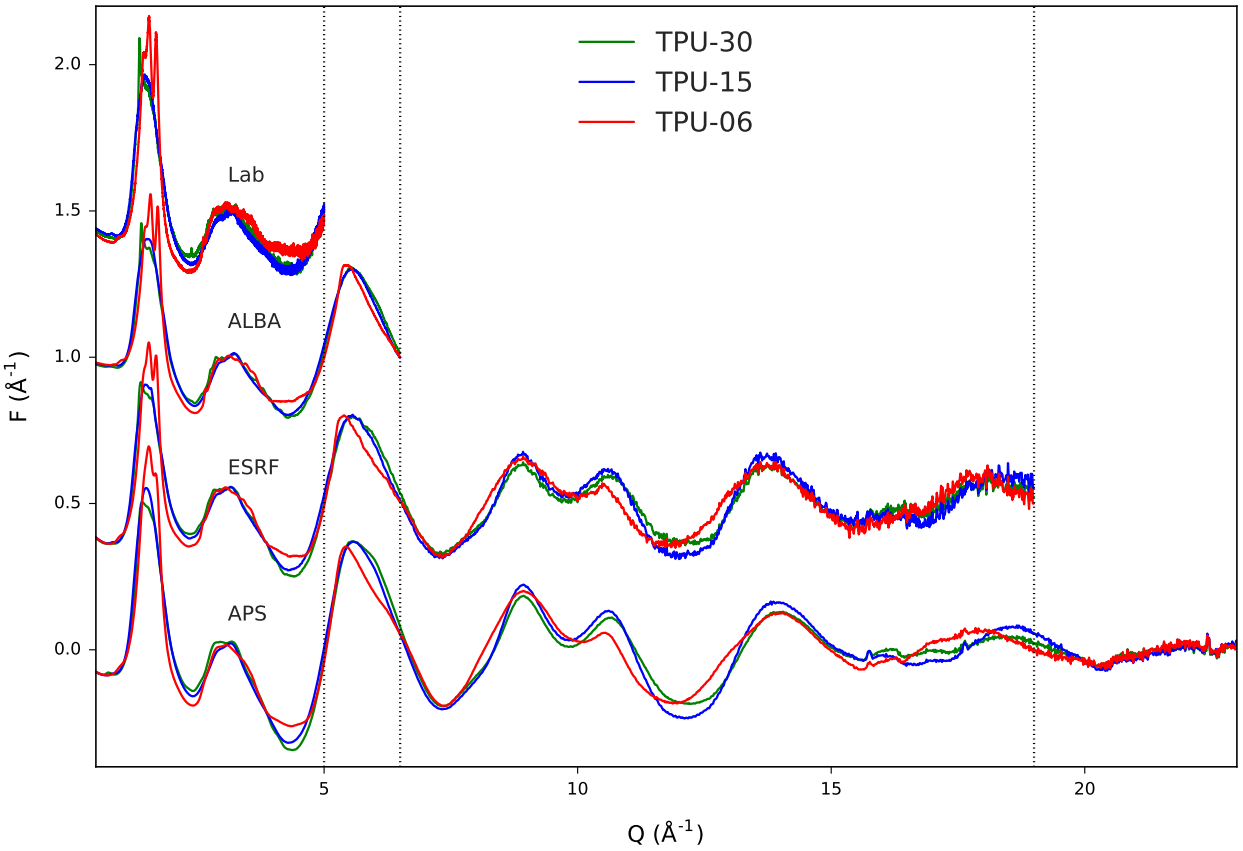

Figure S7: Comparison of the reduced total scattering functions $F(Q)$s obtained by correcting and normalizing the diffraction datasets using xPDFsuite.[15] $F(Q)$s from laboratory (Q_{max} = 5.0 Å) and ALBA measurements (Q_{max} = 6.5 Å^{-1}) were Fourier transformed to obtain the chain packing density distribution functions (DDFs). $F(Q)$s from ESRF (Q_{max} = 19.0 Å^{-1}) and APS (Q_{max} = 23.0 Å^{-1}) were Fourier transformed to obtain the high-resolution pair distribution functions (PDFs) with atomic resolution. Comparison to the high Q_{max} measurements was made to ensure that the corrections used by the PDFGetX3 algorithm did not result in spurious behavior for the limited Q-ranges in the Lab and ALBA data.

4.7 Assessment of local structure in the PDFs

The high real-space resolution PDFs obtained from the total scattering measurements at ESRF (Q_{max} = 19.0 Å^{-1}) and APS (Q_{max} = 23.0 Å^{-1}) are compared in Fig. S11. The

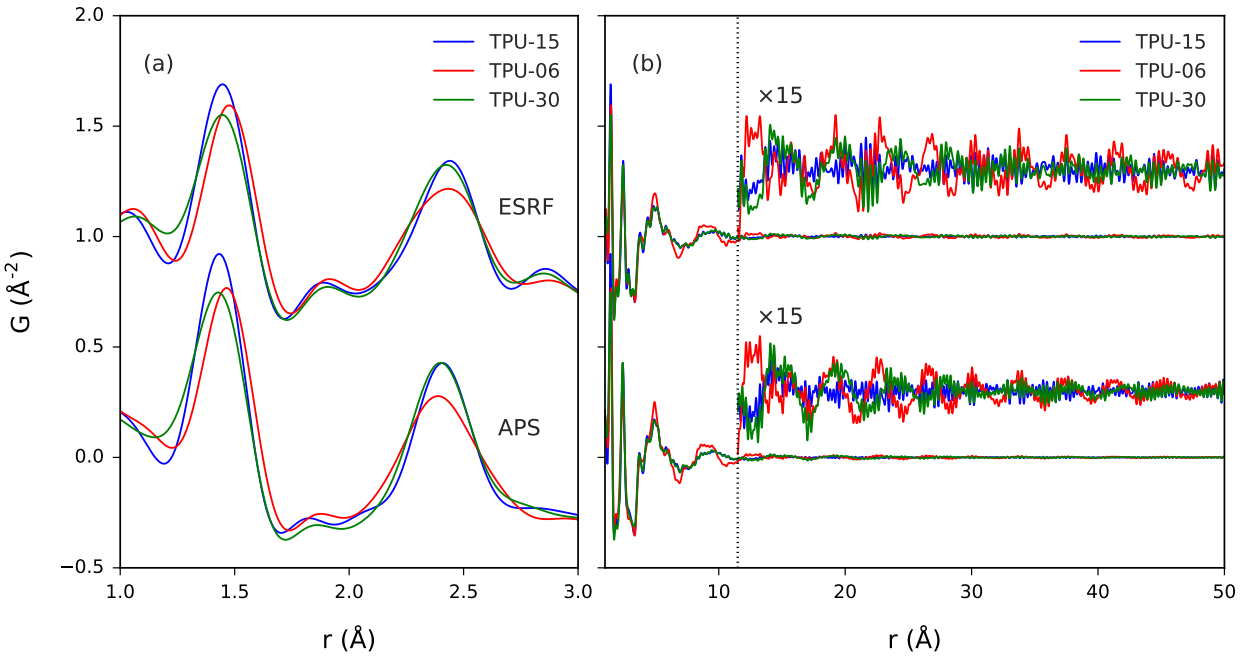

Figure S8: Comparison of high r-resolution PDFs from ESRF and APS over (a) short-distance and (b) long-distance ranges. Long-r data in (b) are amplified to see the signals originating from the small amount of long range ordered content.

average nearest (NN) and next-nearest (NNN) neighbor bond distances in each sample were estimated by the first two sharp peaks in the PDFs, seen in Fig. S11(a). The two peaks were separately fit by $f(r)$, defined by a Gaussian peak with a sloping baseline, i.e.

$$f(r) = a \exp\left[-(r-x)^2/(2\sigma^2)\right] + br + c, \tag{7}$$

where a is a scaling factor, x is the peak position, σ^2 is the variance, and b and c define the sloping baseline. Refinements were performed over ranges of r =1.25–1.70 Å for the NN distance, and r =2.10–2.70 Å for the NNN distance. The results are given in Table S3. Since the single-peak model does not give an accurate representation of the multiple types of contributions (e.g. C-C, C=C, C-O, C=O, C-N, C=N) to the NN and NNN peaks,

Table S3: Parameter values from fitting to the NN and NNN peaks in the high real-space resolution PDFs. It should be noted that this simple single-peak model is not technically correct since NN and NNN correlations have multiple contributions, and are therefore not truly Gaussian in nature. However, it does help to get an approximate measure for average NN and NNN values and to identify significantly deviating behavior, i.e. in the NN position and NNN standard deviation for TPU-06 due to the HDI component.

Sample	Parameter	Peak 1			Peak 2		
		ESRF	APS	Average	ESRF	APS	Average
TPU-15	x (Å)	1.4518(4)	1.4372(6)	1.44(1)	2.439(1)	2.4094(3)	2.42(2)
	σ (Å)	0.1084(7)	0.1029(9)	0.106(4)	0.128(2)	0.1144(4)	0.12(1)
TPU-06	x (Å)	1.4831(4)	1.4735(3)	**1.478(7)**	2.433(2)	2.3874(6)	2.41(3)
	σ (Å)	0.1088(6)	0.1046(5)	0.107(3)	0.203(5)	0.153(1)	**0.18(4)**
TPU-30	x (Å)	1.4577(4)	1.4410(7)	1.45(1)	2.4203(9)	2.3967(2)	2.41(2)
	σ (Å)	0.111(7)	0.1089(11)	0.110(1)	0.144(2)	0.1249(3)	0.13(1)

we further tested molecular models of both monomeric and polymerized chain models in reproducing the different behavior of the short-range intramolecular atom-pair correlations. Monomer and polymer chain models were built and relaxed with the Merck molecular force field MMFF94s.[23] This force field may not give an entirely accurate representation of longer range chain conformations expected in the bulk, particularly for HDI-BD, where we do not have a crystal structure for comparison, but the short-range interatomic distances and dihedral angles are typically well represented. The monomer chain models are shown in Fig. S9 and the polymer chain models are shown in Fig. S10. PDFs were calculated from the individual monomer and polymer chains using Diffpy-CMI.[24] The reduced structure function $F(Q)$ was simulated by the Debye function as

$$F(Q) = \frac{1}{N} \sum_i \sum_{j \neq i} \frac{f_i^* f_j}{\langle f \rangle^2} \frac{\sin Q r_{ij}}{r_{ij}}, \tag{8}$$

and then Fourier transformed using Eq. 4 to get the PDF of the molecule. The model PDFs were simulated with a atomic displacement parameter B_{iso} =0.3 Å^2, Q_{min} =1.5 Å^{-1}, and Q_{max} =23.0 Å^{-1} (the same as the PDFs obtained from APS data for comparison).

Using the PDFs of the monomer chain models in Fig. S9, the TPU signals were approximated by the HSC estimates given in Table 1 in the paper:

1. TPU-15: $G(r) = 0.43 \times [G_{MDI}(r) + G_{BD}(r)]/2 + 0.57 \times G_{Butanol}(r)$
2. TPU-06: $G(r) = 0.46 \times [G_{HDI}(r) + G_{BD}(r)]/2 + 0.54 \times G_{Butanol}(r)$
3. TPU-30: $G(r) = 0.44 \times [G_{MDI}(r) + G_{BD}(r)]/2 + 0.56 \times [G_{ADA}(r) + G_{HDO}(r) + G_{BD}(r)]/3$

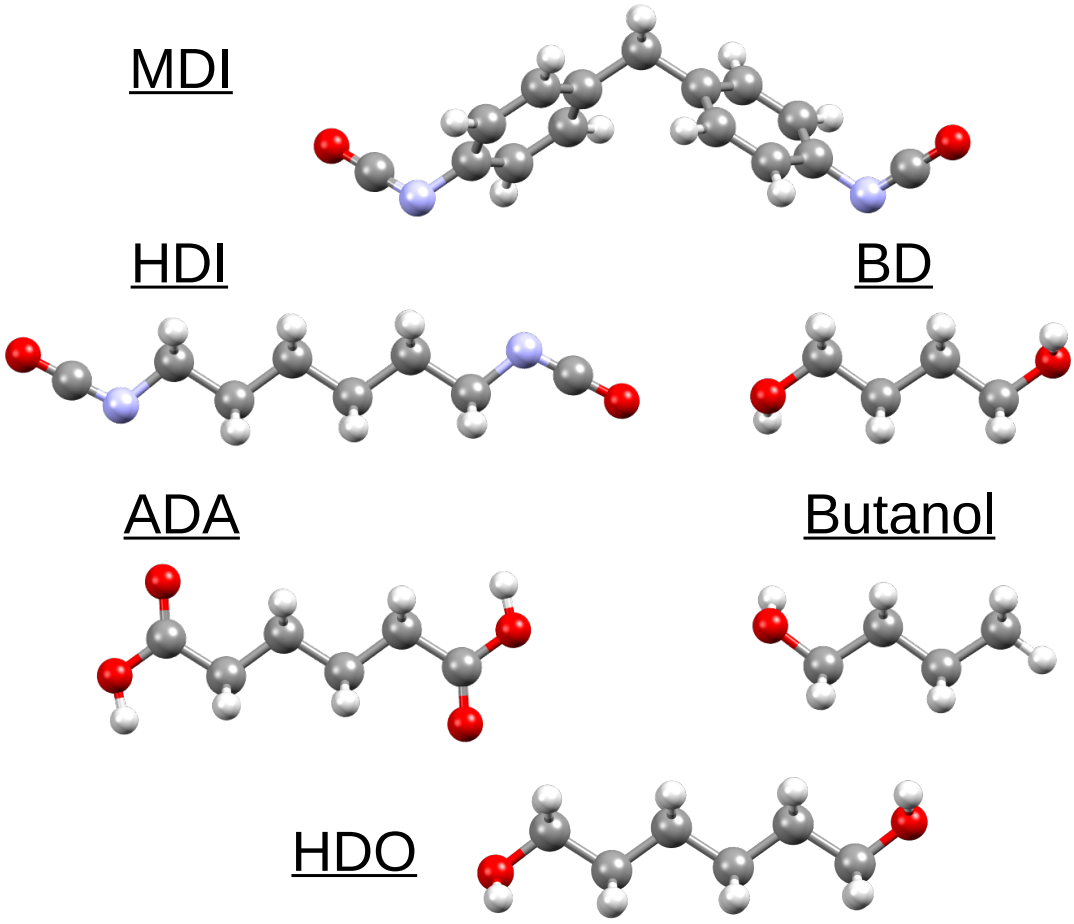

Figure S9: Monomer chain models relaxed by MMFF94s.

The aggregate PDFs for the polymer chain models in Fig. S10 were calculated in the same way:

1. TPU-15: $G(r) = 0.43 \times G_{(MDI-BD)_3}(r) + 0.57 \times G_{(PTHF)_3}(r)$
2. TPU-06: $G(r) = 0.46 \times G_{(HDI-BD)_3}(r) + 0.54 \times G_{(PTHF)_3}(r)$
3. TPU-30: $G(r) = 0.44 \times G_{(MDI-BD)_3}(r) + 0.56 \times G_{(BD-ADA-HDO)}(r)$

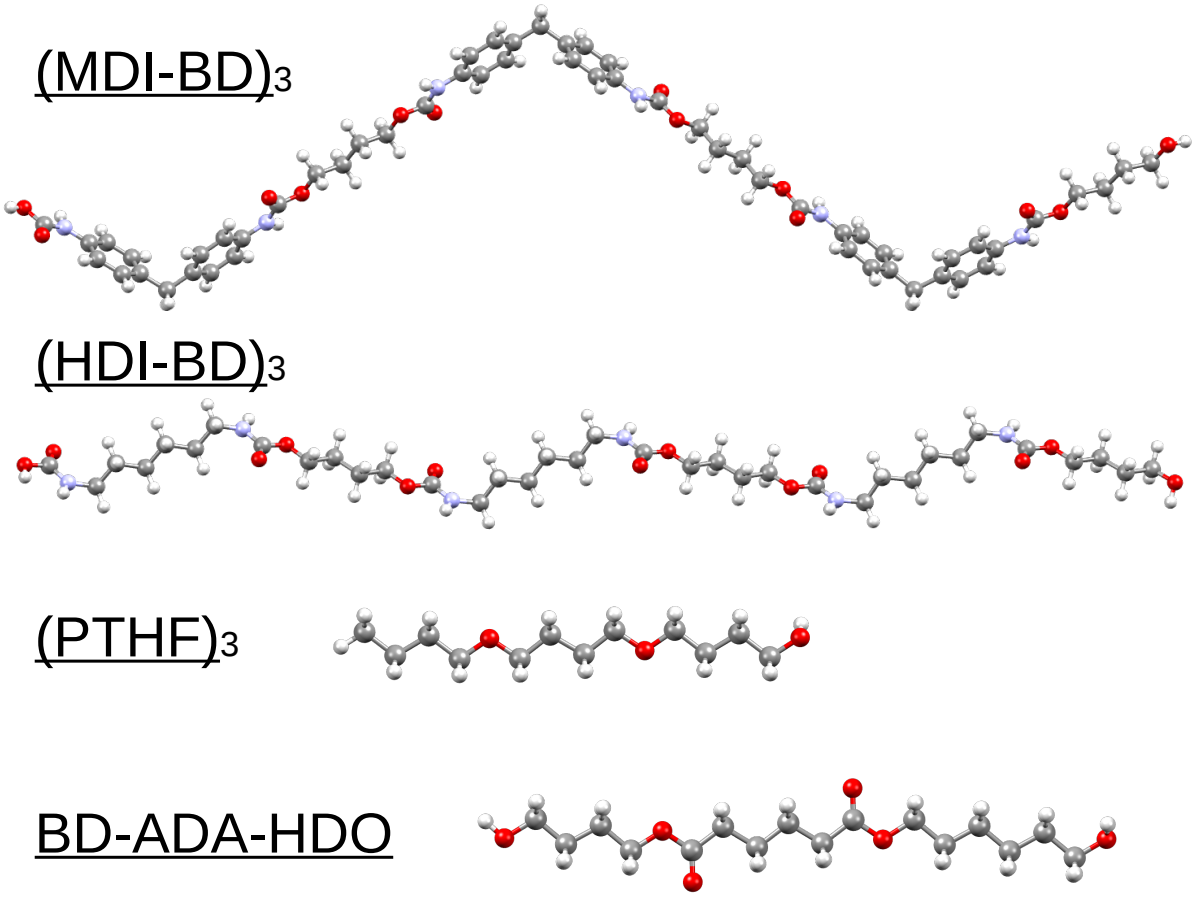

Figure S10: Polymer chain models relaxed by MMFF94s.

The aggregate PDFs for the monomer and polymer chain models were rescaled to match the intensity of the first peak in the corresponding experimental PDF for comparison. The resulting simulated PDFs are compared to the experimental PDFs in Fig. S11. Both models give a fairly good match to the experimental PDFs, although the polymer chain model clearly does better, especially in reproducing the positions, breadths, and relative intensities of the NNN peaks.

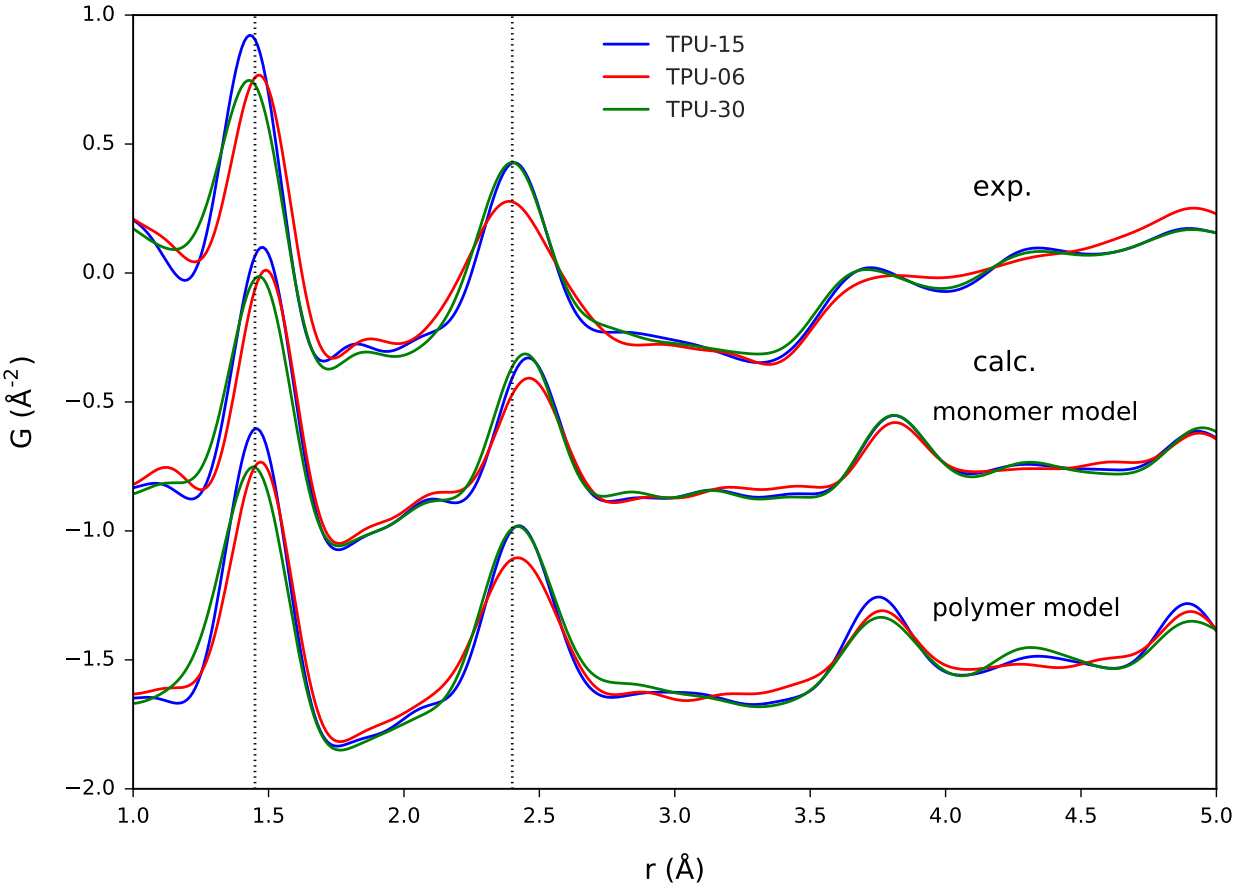

Figure S11: Comparison of the experimental (exp.) PDFs for TPU-15, TPU-06, and TPU-30 to the calculated (calc.) PDFs approximated from the mixed monomer and polymer chain models.

4.8 Experimental resolution effects

A simple way to model the real space damping effect is to refine a structure model to fit the PDF of the standard measurement, including a Gaussian damping factor, where the model is defined as

$$G(r) = G_{\infty}(r) \exp\left[\frac{-\left(rQ_{damp}\right)^2}{2}\right] \tag{9}$$

where $G_{\infty}(r)$ is the PDF with infinite resolution (without instrumental effects). Depending on the resolution function for the instrument, the damping profile may not necessarily be perfectly Gaussian, although this is generally a good approximation.

The Q_{max} used and the Q_{damp} values obtained from refinement of the standard are given for the different TPU datasets in Table S4. Lower Q_{damp} values signify less damping of the real-space PDF or DDF, and therefore, the ability to view structure signals up to longer distances in real-space. The resulting damping envelopes from the APS and ESRF measurements are compared to the lab measurements in Figure Fig. S12, to give an idea of the effective distances over which structure can be resolved in the measured PDFs. The lab measurement standard consists of the 10% Si puck made to reproduce the same sample geometry of the TPU pellets. A second lab measurement of a thin layer of Si powder is given for reference, which shows the best resolution measureable for a thinner sample in transmission with this diffractometer.

Table S4: List of samples. *For the ALBA measurements, a standard with similar geometry was not measured.

Value	Lab	ALBA	ESRF	APS
Q_{max} Å^{-1}	5.0	6.5	19.0	22.0
Q_{damp} Å^{-1}	0.012	-*	0.018	0.040

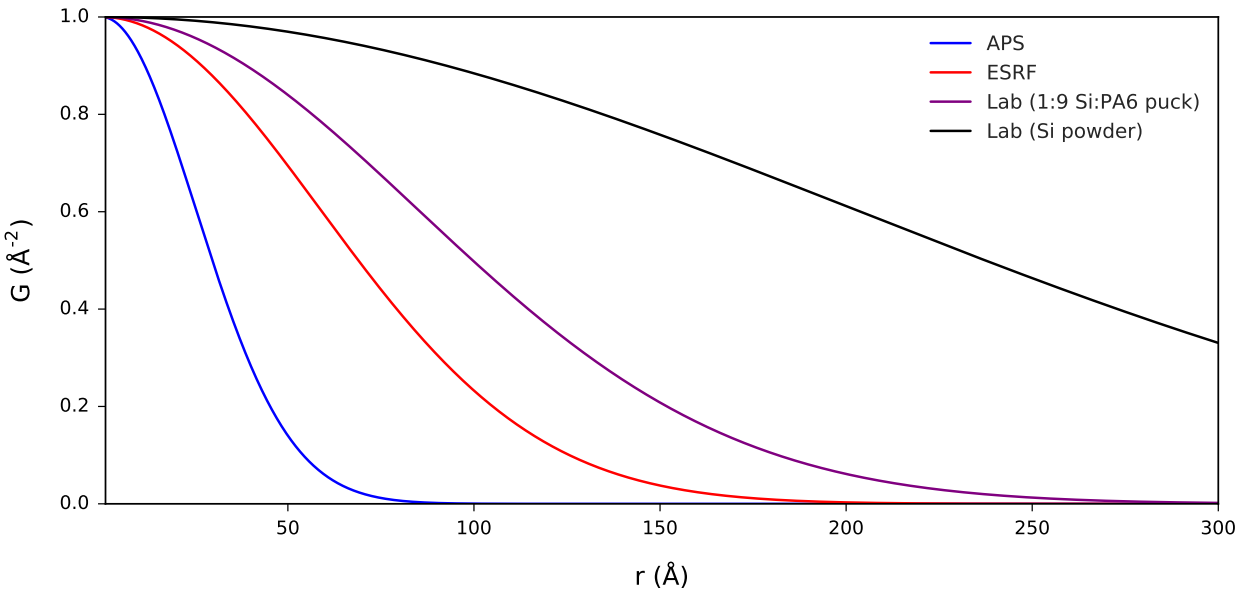

Figure S12: Real-space damping profiles determined by fitting standards, CeO_2 for synchrotron measurements, and Si for laboratory measurements.

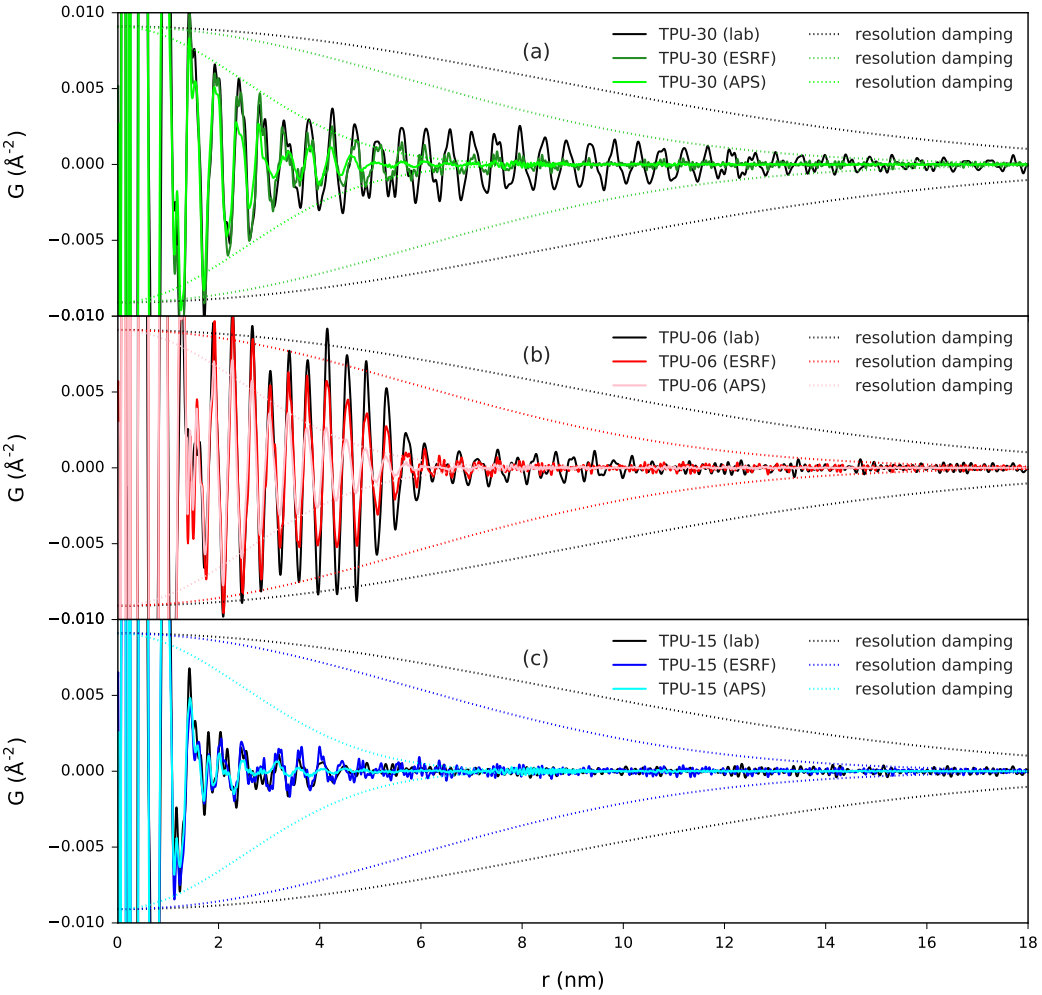

Figure S13: The long-r structure signals in the PDFs from data collected at ESRF and APS are compared to the DDF signals obtained from the higher Q-space resolution (but lower real-space resolution) laboratory measurements using CuKα_1 radiation for (a) TPU-30, (b) TPU-06, and (c) TPU-15. The peak positions and relative amplitudes are consistent between all datasets, indicating that the laboratory DDFs are not significantly impaired by effects due to low Q_{max} or instrumental profile for these samples. For the comparisons here Lorch modification functions were used to reduce high frequency termination effects in the synchrotron data with $Q_{max} = 12$ and 15 Å^{-1} for the ESRF and APS data respectively.

4.9 Estimation of PDF attenuation profiles from AFM

In the PDF analysis, the attenuation of the DDF profiles were highlighted as characteristic of the aggregate domain size and shape distribution. To compare the domain dimensions obtained from AFM image analysis to the DDF results, an attenuation profile was approximated from the distribution of minimum and maximum Feret diameters. This was performed by assuming a spherical distribution for every length, where the damping function for a sphere is defined as

$$\gamma_{sphere}(r, d_c) = \left[1 - \frac{3r}{2d_c} + \frac{1}{2}\left(\frac{r}{d_c}\right)^3\right] H(d_c - r) \tag{10}$$

where d_c is the coherent domain diameter, and $H(d_c - r)$ is a step function with value 1 for $r \leq d_c$ and 0 for $r > d_c$. It is important to note that analytical forms for other damping profiles exist, such as oblate and prolate spheroids, sheets, and cylinders.[25–28] In fact, depending on the morphology of the hard and soft phases, the damping profile could be much more complicated, and therefore we test only spherical profiles for simplicity (note: spherical profiles often work well for determining an average value, even if the morphology is not spherical, or there is a distribution). The damping profiles were then estimated by summing over the set of N Feret diameters determined from the AFM images as

$$\gamma_{AFM}(r) = \sum_{i}^{N} \gamma_{sphere}(r, d_{c_i}). \tag{11}$$

5 Solid-state nuclear magnetic resonance (SSNMR)

^{13}C-detected ^{1}H–^{1}H spin-diffusion solid-state NMR spectra build-ups were recorded on a 7 Tesla (300 MHz ^{1}H resonance frequency) Bruker Avance 1 solid-state NMR spectrometer equipped with a double-resonance magic-angle spinning probe. Disks were cut out of TPU samples, to fit into 7 mm ZrO_2 rotors with Kel-F caps. NMR experiments were performed under 298 K at 5700 Hz sample spinning. In line with previous studies,[29–31] ^{1}H was polarized by a 90°-pulse, followed by a dipolar filter for relaxing magnetization on the hard phase, a variable longitudinal spin-diffusion delay, and 1 ms Hartmann-Hahn cross-polarization to ^{13}C. For each sample, 13 increments of spin diffusion time with 6144 scans were recorded. Each experiment had a run time of ∼2 days. Furthermore, experiments for correction of T_1-relaxation effects were recorded and used to process the spin-diffusion buildups.

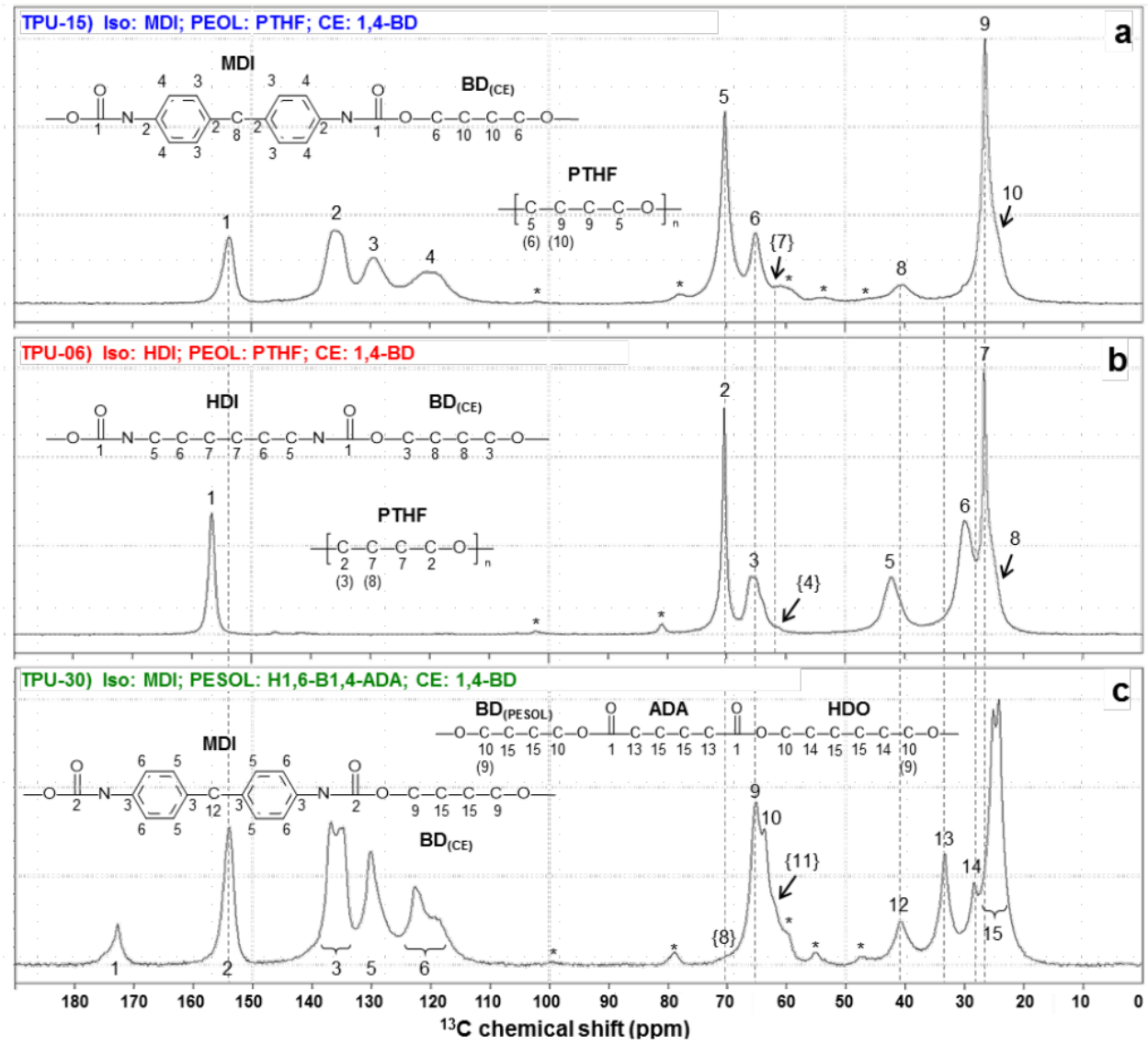

Figure S14: ^{13}C solid-state NMR spectra from 1 ms ^{1}H-^{13}C cross-polarization for (a) TPU-15, (b) TPU-06, and (c) TPU-30. Asterisks (∗) denote spinning side-bands. Resonances numbered in curly brackets remained unassigned; note that they do not contribute substantial signal. Assignments in round brackets () denote overlapping resonances, which are assigned with confidence.

References

(1) Schneider, C. A.; Rasband, W. S.; Eliceiri, K. W. NIH Image to ImageJ: 25 years of image analysis. *Nat. Methods* **2012**, *9*, 671–675.

(2) Wagner, T.; Eglinger, J. (2017, June 28). thorstenwagner/ij-particlesizer: v1.0.9 Snapshot release (Version v1.0.9-SNAPSHOT). Zenodo. http://doi.org/10.5281/zenodo.820296.

(3) Reinhold, C.; Fischer, E. W.; Peterlin, A. Evaluation of small-angle x-ray scattering of polymers. *J. Appl. Phys.* **1964**, *35*, 71–74.

(4) Ruland, W. The evaluation of the small-angle scattering of lamellar two-phase systems by means of interface distribution functions. *Colloid Polym. Sci.* **1977**, *255*, 417–427.

(5) Stribeck, N.; Ruland, W. Determination of the interface distribution function of lamellar two-phase systems. *J. Appl. Crystallogr.* **1978**, *11*, 535–539.

(6) Wang, Z.-G.; Hsiao, B. S.; Murthy, N. S. Comparison of intensity profile analysis and correlation function methods for studying the lamellar structures of semicrystalline polymers using small-angle x-ray scattering. *J. Appl. Crystallogr.* **2000**, *33*, 690–694.

(7) Laity, P. R.; Taylor, J. E.; Wong, S. S.; Khunkamchoo, P.; Norris, K.; Cable, M.; Andrews, G. T.; Johnson, A. F.; Cameron, R. E. A review of small-angle scattering models for random segmented poly(ether-urethane) copolymers. *Polymer* **2004**, *45*, 7273–7291.

(8) Koberstein, J. T.; Stein, R. S. Small-angle X-ray scattering studies of microdomain structure in segmented polyurethane elastomers. *J. Polym. Sci. Pol. Phys.* **1983**, *21*, 1439–1472.

(9) Cser, F. About the Lorentz correction used in the interpretation of small angle x-ray scattering data of semicrystalline polymers. *J. Appl. Polym. Sci.* **2001**, *80*, 2300–2308.

(10) Stribeck, N. *X-ray scattering of soft matter*; Springer-Verlag: Berlin Heidelberg, 2007.

(11) Méring, J.; Tchoubar, D. Interprétation de la diffusion centrale des rayons X par les systèmes poreux. I. *J. Appl. Crystallogr.* **1968**, *1*, 153–165.

(12) Vonk, C. G.; Kortleve, G. X-ray small-angle scattering of bulk polyethylene. *Colloid Polym. Sci.* **1967**, *220*, 19–24.

(13) Gille, W. Chord length distributions and small-angle scattering. *Eur. Phys. J. B* **2000**, *17*, 371–383.

(14) Gommes, C. J. Small-angle scattering and scale-dependent heterogeneity. *J. Appl. Crystallogr.* **2016**, *49*, 1162–1176.

(15) Yang, X.; Juhás, P.; Farrow, C.; Billinge, S. J. L. xPDFsuite: an end-to-end software solution for high throughput pair distribution function transformation, visualization and analysis. *arXiv* **2015**, 1402.3163.

(16) Chupas, P. J.; Qiu, X.; Hanson, J. C.; Lee, P. L.; Grey, C. P.; Billinge, S. J. L. Rapid acquisition pair distribution function analysis (RA-PDF). *J. Appl. Crystallogr.* **2003**, *36*, 1342–1347.

(17) Kieffer, J.; Ashiotis, G.; Deschildre, A.; Nawaz, Z.; Wright, J. P.; Karkoulis, D.; Picca, F. E. The fast azimuthal integration Python library: pyFAI. *J. Appl. Crystallogr.* **2015**, *48*, 510–519.

(18) Juhás, P.; Davis, T.; Farrow, C. L.; Billinge, S. J. L. PDFgetX3: A rapid and highly automatable program for processing powder diffraction data into total scattering pair distribution functions. *J. Appl. Crystallogr.* **2013**, *46*, 560–566.

(19) Farrow, C. L.; Billinge, S. J. L. Relationship between the atomic pair distribution function and small angle scattering: implications for modeling of nanoparticles. *Acta Crystallogr. A* **2009**, *65*, 232–239.

(20) Lorch, E. Neutron diffraction by germania, silica and radiation-damaged silica glasses. *J. Phys. Part C Solid* **1969**, *2*, 229–237.

(21) Farrow, C. L.; Juhás, P.; Liu, J.; Bryndin, D.; Božin, E. S.; Bloch, J.; Proffen, T.; Billinge, S. J. L. PDFfit2 and PDFgui: Computer programs for studying nanostructure in crystals. *J. Phys: Condens. Mat.* **2007**, *19*, 335219.

(22) Coelho, A. A. TOPAS and TOPAS-Academic: an optimization program integrating computer algebra and crystallographic objects written in C++. *J. Appl. Crystallogr.* **2018**, *51*, 210–218.

(23) Halgren, T. A. MMFF VI. MMFF94s option for energy minimization studies. *J. Comput. Chem.* **1999**, *20*, 720–729.

(24) Juhás, P.; Farrow, C. L.; Yang, X.; Knox, K. R.; Billinge, S. J. L. Complex Modeling: a strategy and software program for combining multiple information sources to solve ill-posed structure and nanostructure inverse problems. *Acta Crystallogr. A* **2015**, *71*, 562–568.

(25) Howell, R. C.; Proffen, T.; Conradson, S. D. Pair distribution function and structure factor of spherical particles. *Phys. Rev. B* **2006**, *73*, 094107.

(26) Lei, M.; de Graff, A. M. R.; Thorpe, M. F.; Wells, S. A.; Sartbaeva, A. Uncovering the intrinsic geometry from the atomic pair distribution function of nanomaterials. *Phys. Rev. B* **2009**, *80*, 024118.

(27) Kodama, K.; Iikubo, S.; Taguchi, T.; Shamoto, S. Finite size effects of nanoparticles on the atomic pair distribution functions. *Acta Crystallogr. A* **2006**, *62*, 444–453.

(28) Gamez, L.; Terban, M. W.; Billinge, S. J. L.; Martinez-Inesta, M. Modelling and validation of particle size distributions of supported nanoparticles using the pair distribution function technique. *J. Appl. Crystallogr.* **2017**, *50*, 741–748.

(29) Clauss, J.; Schmidt-Rohr, K.; Spiess, H. Determination of domain sizes in heterogeneous polymers by solid-state NMR. *Acta Polymer.* **1993**, *44*, 1–17.

(30) Servay, T.; Voelkel, R.; Schmiedberger, H.; Lehmann, S. Thermal oxidation of the methylene diphenylene unit in MDI-TPU. *Polymer* **2000**, *41*, 5247–5256.

(31) Schmidt-Rohr, K.; Spiess, H. W. *Multidimensional Solid-State NMR and Polymers*; Academic Press: London, 1994.